

1  
2  
3  
4  
5  
6  
7  
8  
9  
10  
11  
12  
13  
14  
15  
16  
17  
18  
19  
20  
21  
22  
23  
24  
25  
26

**Earthquakes Drive Focused Denudation along  
a Tectonically Active Mountain Front**

Gen Li<sup>1\*</sup>, A. Joshua West<sup>1</sup>, Alexander L. Densmore<sup>2</sup>, Zhangdong Jin<sup>3</sup>, Fei Zhang<sup>3</sup>, Jin Wang<sup>3</sup>, Marin Clark<sup>4</sup>, and Robert G. Hilton<sup>2</sup>

<sup>1</sup>Department of Earth Sciences, University of Southern California, Los Angeles, CA 90089, USA

<sup>2</sup>Institute of Hazard, Risk and Resilience and Department of Geography, Durham University, Durham DH1 3LE, UK

<sup>3</sup>State Key Laboratory of Loess and Quaternary Geology, Institute of Earth Environment, Chinese Academy of Sciences, Xi'an 710075, China

<sup>4</sup>Department of Earth and Environmental Sciences, University of Michigan, Ann Arbor, MI 48109, USA

\* corresponding author  
Phone: +1-(213)740-5825  
Email: genli@usc.edu

Manuscript in revision for *Earth and Planetary Science Letters*

27 **Abstract**

28 Earthquakes cause widespread landslides that can increase erosional fluxes observed  
29 over years to decades. However, the impact of earthquakes on denudation over the  
30 longer timescales relevant to orogenic evolution remains elusive. Here we assess  
31 erosion associated with earthquake-triggered landslides in the Longmen Shan range at  
32 the eastern margin of the Tibetan Plateau. We use the  $M_w$  7.9 2008 Wenchuan and  $M_w$   
33 6.6 2013 Lushan earthquakes to evaluate how seismicity contributes to the erosional  
34 budget from short timescales (annual to decadal, as recorded by sediment fluxes) to  
35 long timescales (kyr to Myr, from cosmogenic nuclides and low temperature  
36 thermochronology). Over this wide range of timescales, the highest rates of  
37 denudation in the Longmen Shan coincide spatially with the region of most intense  
38 landsliding during the Wenchuan earthquake. Across sixteen gauged river catchments,  
39 sediment flux-derived denudation rates following the Wenchuan earthquake are  
40 closely correlated with seismic ground motion and the associated volume of  
41 Wenchuan-triggered landslides ( $r^2 > 0.6$ ), and to a lesser extent with the frequency of  
42 high intensity runoff events ( $r^2 = 0.36$ ). To assess whether earthquake-induced  
43 landsliding can contribute importantly to denudation over longer timescales, we  
44 model the total volume of landslides triggered by earthquakes of various magnitudes  
45 over multiple earthquake cycles. We combine models that predict the volumes of  
46 landslides triggered by earthquakes, calibrated against the Wenchuan and Lushan  
47 events, with an earthquake magnitude-frequency distribution. The long-term,  
48 landslide-sustained “seismic erosion rate” is similar in magnitude to regional  
49 long-term denudation rates ( $\sim 0.5\text{-}1 \text{ mm yr}^{-1}$ ). The similar magnitude and spatial  
50 coincidence suggest that earthquake-triggered landslides are a primary mechanism of  
51 long-term denudation in the frontal Longmen Shan. We propose that the location and  
52 intensity of seismogenic faulting can contribute to focused denudation along a  
53 high-relief plateau margin.

54 **1. Introduction**

55 Mountain erosion affects rates and patterns of crustal deformation including  
56 seismogenic faulting [e.g., Steer et al., 2014] and flexural-isostatic responses [e.g.,  
57 Molnar and England, 1990], and influences the geological carbon cycle and  
58 consequently the climate system [e.g., Raymo et al., 1988; Wang et al., 2016]. Large  
59 earthquakes are thought to play an important role in the denudation of  
60 tectonically-active mountain ranges because they cause widespread landslides that  
61 generate large volumes of clastic sediment [Keefer, 1994; Larsen et al., 2010; Hovius  
62 et al., 2011; Parker et al., 2011; Wang et al., 2015a]. Delivery of landslide debris to  
63 rivers and the subsequent fluvial evacuation can increase erosion rates over years to  
64 decades [e.g., Hovius et al., 2011; Wang et al., 2015a]. However, over longer  
65 timescales relevant to orogenic evolution ( $10^4$ - $10^6$  yr), the role of earthquakes in  
66 denudation remains less well constrained, even though the volume of seismically  
67 triggered landslides may be sufficient to partly or wholly counteract seismically  
68 induced rock uplift [Parker et al., 2011; Hovius et al., 2011; Li et al., 2014; Marc et al.,  
69 2016a].

70  
71 Detailed mapping of landslides [e.g., Keefer, 1994; Parker et al., 2011; Li et al., 2014;  
72 Xu et al., 2015] and hydrological gauging of sediment fluxes [e.g., Hovius et al., 2011;  
73 Wang et al., 2015a] capture the aftermath of individual events. Across multiple events,  
74 landslide volume scales with earthquake magnitude [Keefer, 1994; Malamud et al.,  
75 2004; Marc et al., 2016b]. Combined with return time statistics for earthquakes, this  
76 scaling relationship can yield an estimate of long-term landslide rate that should  
77 reflect a “seismic erosion rate” associated with repeated earthquakes, assuming fluvial  
78 evacuation of landslide debris [Keefer, 1994; Malamud et al., 2004; Lav é and  
79 Burbank, 2004; Li et al., 2014; Marc et al., 2016a]. Keefer (1994) found that seismic  
80 erosion rates are comparable to fluvial sediment yields measured in several regions.  
81 Cosmogenic nuclide and thermochronology datasets allow us to expand this approach  
82 to consider denudation rates measured over longer timescales that encompass multiple  
83 earthquakes and that are more relevant to mountain belt evolution. In this study, we  
84 focus on the Longmen Shan region of central China, where the 2008  $M_w$  7.9  
85 Wenchuan and 2013  $M_w$  6.6 Lushan earthquakes allow us to make estimates of  
86 seismic erosion rates. We evaluate both the spatial distribution and magnitude of these  
87 rates in the context of datasets from fluvial sediment fluxes, cosmogenic nuclides, and  
88 low-temperature thermochronology [e.g., Kirby et al., 2002; Ouimet et al., 2009;  
89 Godard et al., 2010; Liu-Zeng et al., 2011; Wang et al., 2015a].

90  
91 The steep Longmen Shan mountain range defines the eastern margin of the Tibetan  
92 Plateau. This region has been at the nexus of contentious debates over the importance  
93 of motion along shallow faults versus ductile flow of lower crust for collisional  
94 mountain building [e.g., Clark and Royden, 2000; Hubbard and Shaw, 2009]. Focused  
95 denudation along the steep topographic front of such plateau margins may exert an  
96 important influence on deformation [e.g., Beaumont et al., 2001]. However, the  
97 relative roles of tectonic and climatic drivers of denudation – and thus the link

98 between climate and the geodynamic processes – remain unresolved, both for the  
99 Longmen Shan [e.g., Ouimet et al., 2009; Godard et al., 2010; Liu-Zeng et al., 2011]  
100 and elsewhere. We aim to gain new general insight into the long-term role of seismic  
101 erosion in tectonically active mountains and how it may contribute to focused  
102 denudation along the eastern margin of the Tibetan plateau.

103

## 104 **2. Setting**

105 With elevations rising to higher than 5 km over a 50 km horizontal distance, the  
106 eastern Longmen Shan flank represents one of Earth's steepest plateau margins [Clark  
107 and Royden, 2000; Densmore et al., 2007; Burchfiel et al., 2008]. Several Yangtze  
108 headwater rivers (mainly the Min Jiang, Fu Jiang, Tuo Jiang, Qingyi Jiang and Dadu  
109 He) drain from the Longmen Shan into the Sichuan Basin (Figure 1a). A series of  
110 dextral-thrusting, oblique-slip faults bound the mountain front and comprise the  
111 Longmen Shan fault system [Densmore et al., 2007; Burchfiel et al., 2008]. The  
112 bedrock geology consists mainly of Proterozoic basement granitoids and high-grade  
113 metamorphic rocks, metamorphosed sedimentary rocks of a Paleozoic passive margin  
114 sequence, unmetamorphosed sedimentary rocks associated with a Mesozoic  
115 foreland-basin succession, and limited Cenozoic sediments [Burchfiel et al., 2008].  
116 Climatically, the Longmen Shan range is located at the transition between the  
117 domains dominated by the east Asian monsoon and the westerlies. Across the  
118 Longmen Shan, average annual rainfall decreases from the margin ( $\sim 1100 \text{ mm yr}^{-1}$ )  
119 towards the plateau (as low as  $\sim 600 \text{ mm yr}^{-1}$ ) [Liu-Zeng et al., 2011]. This regional  
120 climate pattern is largely determined by the high topography, which acts as an  
121 orographic barrier and may also affect atmospheric circulation by heating of the  
122 atmosphere [Molnar et al., 2010 and references therein]. Precipitation is highly  
123 seasonal, with most rainfall during the wet season from June to September.

124

125 The  $M_w$  7.9 Wenchuan earthquake on May 12<sup>th</sup>, 2008 initiated in the southern  
126 Longmen Shan, near the town of Yingxiu, and ruptured northeastward for  $\sim 270$  km  
127 along the Longmen Shan fault system (Figure 1a) [Burchfiel et al., 2008; Shen et al.,  
128 2009]. The strong ground motion triggered  $> 56,000$  landslides in the steep  
129 mountainous topography (Figure 1a) [Parker et al., 2011; Li et al., 2014; Xu et al.,  
130 2014]. These seismically induced landslides introduced large volumes of clastic  
131 sediment into the fluvial system, estimated to total  $\sim 3 \text{ km}^3$  [Li et al., 2014]. Prior  
132 work has aimed to understand the effects on sediment transport. Li et al. (2014)  
133 documented the spatial pattern and volume of landsliding, and Li et al. (2016)  
134 assessed the connectivity of these landslides to the river network as a means of  
135 understanding their behavior as sediment sources. Wang et al. (2015a) used data from  
136 the Chinese Hydrology Bureau to quantify suspended sediment transport rates. After  
137 the Wenchuan earthquake (2008-2012), suspended sediment fluxes from the Min  
138 Jiang, Fu Jiang and Tuo Jiang catchments increased by 3 to 7 times compared to  
139 pre-earthquake levels (2006-2007). Based on  $^{10}\text{Be}$  concentrations in quartz from Min  
140 Jiang riverbed sands, West et al. (2014) suggested that bedload transport rates had  
141 increased by a similar order of magnitude to those of suspended load. The present

142 study takes advantage of this prior work, including the landslide inventory and  
143 sediment fluxes, in order to compare spatial patterns of denudation across a range of  
144 timescales.

145

146 We use the  $M_w$  6.6 Lushan event as an additional constraint on the magnitude of  
147 seismic erosion rates. The Lushan earthquake occurred on April 20<sup>th</sup>, 2013 in the  
148 southern Longmen Shan, 80 km south of the Wenchuan epicenter (Figure 1a). This  
149 event initiated on a ramp in the range-front blind thrust fault, in the footwall of the  
150 Wenchuan rupture [Wang et al., 2014]. As in the Wenchuan event, widespread  
151 landsliding occurred in the southern Longmen Shan range during the Lushan  
152 earthquake. Xu et al. (2015) reported more than 20,000 co-seismic landslides, with a  
153 total area of 18.88 km<sup>2</sup> and an estimated volume of 0.042 km<sup>3</sup> across the region of the  
154 Lushan earthquake.

155

### 156 **3. Materials and Approaches**

#### 157 **3.1. Landslide inventory**

158 For the Wenchuan earthquake, co-seismic and immediately post-seismic landslides  
159 (within six months after the earthquake) were mapped by Li et al. (2014). Landslide  
160 volumes were calculated from empirical landslide area-volume scaling relations [e.g.,  
161 Larsen et al., 2010]. We assume that mapped landslides mainly resulted from the  
162 Wenchuan mainshock because we find that aftershocks contributed <5% of the total  
163 seismic moment release across the Longmen Shan, based on the seismic catalog  
164 spanning over six months following the mainshock [CSN Catalog, 2015]. This finding  
165 is consistent with observations from other earthquakes that suggest most landslides  
166 occur during the main shock [e.g., Roback et al., 2017]. Additional volume associated  
167 with post-seismic (e.g., storm-triggered) landslides is likely to be on the order of a  
168 few percent of the total landslide volume [Li et al., 2016 and references therein].

169

170 For the landslides triggered by the Lushan earthquake, we refer to the landslide  
171 inventory compiled by Xu et al. (2015), who also used empirical scaling relationships  
172 reported in Larsen et al. (2010) to estimate volumes from a landslide map based on  
173 satellite imagery. Xu et al. (2015) mapped Lushan landslides using images collected  
174 from April – May 2013, around five years after the Wenchuan earthquake but  
175 immediately after the Lushan event. Also, there is not much overlap between the  
176 mapping extents and the intensive shaking zones for the Lushan and Wenchuan events  
177 [Li et al., 2014; Xu et al., 2015]. Thus we expect limited influence on the mapped  
178 Lushan landslides from the Wenchuan earthquake.

179

#### 180 **3.2. Geomorphic characterization**

181 In evaluating the spatial patterns of denudation in the Wenchuan region, we focus on  
182 three main catchments (Min Jiang, Fu Jiang and Tuo Jiang), comprising sixteen  
183 sub-catchments as delineated by Li et al. (2016) (Figure 1b and Table S1). SRTM30  
184 digital elevation model (DEM) data have incomplete coverage of the study region, so  
185 we used void-filled SRTM90 DEM data for topographic analysis [Jarvis et al., 2008].

186 Slopes were calculated using standard algorithms provided in the ArcGIS platform  
187 (Figure 1d). Although the derived slopes vary as a function of DEM resolution [e.g.,  
188 Larsen et al., 2014], the biases are systematic (e.g., Figure S1) so we expect little  
189 influence on the relative trends between different catchments. Relief was determined  
190 as the ranges of elevations in 2.5 km-radius and 5 km-radius circular windows. We  
191 also calculated the volumetric density of landslides ( $\text{m}^3 \text{km}^{-2}$ , landslide volume per  
192 unit catchment area) within each studied catchment (Table S1) and along a swath  
193 profile A-A' (Figure 1f). We derived channel steepness indexes ( $k_{sn}$ , normalized to  $\theta_{ref}$   
194 = 0.45, cf. Ouimet et al., 2009; symbol notation listed in Table 1) using the Stream  
195 Profiler toolbox (<http://www.geomorphtools.org>). DEM cells with drainage area < 1  
196  $\text{km}^2$  were excluded to remove colluvial landscapes [Li et al., 2016]. To characterize  
197 ground motion associated with the Wenchuan earthquake, we used gridded peak  
198 ground acceleration (PGA) data obtained from the USGS ShakeMap (USGS Hazard  
199 Program, <http://earthquake.usgs.gov/earthquakes>).

200

### 201 **3.3. Hydrological data**

202 Wang et al. (2015a) analyzed data from the Chinese Hydrology Bureau and calculated  
203 total suspended load fluxes and runoff from 16 gauging stations across the Longmen  
204 Shan catchments (Figure 1a). This data covered both the pre-Wenchuan (2006-2007)  
205 and the post-Wenchuan (2008-2012) time periods. Using this dataset, Li et al. (2016)  
206 derived the suspended load fluxes for sub-catchments, by taking the differences  
207 between fluxes gauged at one station and all neighboring upstream stations, following  
208 a mass balance principle [Li et al., 2016]. Three sub-catchments yielded negative  
209 sediment fluxes, attributed to large sedimentary sinks such as reservoirs. As in Li et al.  
210 (2016), these were excluded from analysis (catchments labeled as “N.A.” in Figure  
211 1b).

212

213 Based on the gauged discharge and catchment area, we derived annual runoff for  
214 sub-catchments using an analogous mass balance approach to that for calculating  
215 sediment fluxes. Wang et al. (2015a) suggested that high magnitude runoff events play  
216 an important role in post-Wenchuan suspended sediment transport. We explored  
217 different thresholds for high magnitude runoff and found that a  $6 \text{ mm day}^{-1}$  threshold  
218 best correlated with denudation rates (Figure S2 in Supporting Information), close to  
219 the  $5 \text{ mm day}^{-1}$  used by Wang et al. (2015a). We also calculated specific stream power  
220 ( $\omega$ ) adopting the approach of Burbank et al. (2003) (details in Supporting Information)  
221 using our compiled runoff and topography data.

222

### 223 **3.4. Calculation of sediment flux-derived (“short term”) denudation rates**

224 The total mass flux from a river catchment (i.e., the denudation rate) includes  
225 suspended, bedload, and dissolved load. To calculate total denudation rates, we  
226 adopted the approach of Liu-Zeng et al. (2011), who determined a pre-Wenchuan  
227 earthquake ratio of dissolved load to suspended load of  $19 \pm 6\%$ , and a ratio of bedload  
228 to suspended load of  $25 \pm 15\%$ . After the earthquake (2009-2012), Jin et al. (2016)  
229 measured solute fluxes at two sites (Zhenjianguan and Weizhou, Figure 1a) in the

230 Min Jiang catchment, yielding a post-earthquake dissolved:suspended load ratio of  
231  $19 \pm 7\%$  (Table S3 and text in Supporting Information), similar to pre-earthquake  
232 estimates. Measurements of  $^{10}\text{Be}$  concentrations in detrital quartz from bed sediments  
233 collected in 2009-2010 [West et al., 2014] indicate that, after the earthquake, bedload  
234 increased by a similar factor as suspended load. Thus the bedload:suspended load  
235 ratio is likely to be similar to that reported prior to the earthquake, i.e.,  $25 \pm 15\%$ .  
236 Using these ratios between the dissolved load, bedload and suspended load, we  
237 calculated total denudation fluxes ( $\text{t yr}^{-1}$ ) from the suspended sediment fluxes and  
238 converted these to denudation rates ( $\text{mm yr}^{-1}$ ), assuming material density of  $2.65 \times 10^3$   
239  $\text{kg m}^{-3}$  [cf. Liu-Zeng et al., 2011]. To account for low-relief, frontal plains, which are  
240 expected to contribute little to the denudation flux, we normalized the calculated  
241 denudation rates to the fraction of mountainous area (defined as areas  $> 800$  m  
242 elevation) in each catchment (Figure 1b and Table S1). We have examined  
243 relationships between these denudation rates and various hydrological and  
244 topographic metrics we have calculated for the Longmen Shan (Section 3.2, 3.3).

245

### 246 **3.5. Compilation of long-term (kyr to Myr) denudation rates**

247 To characterize the denudation of the Longmen Shan over longer timescales, we  
248 compiled  $^{10}\text{Be}$ -derived catchment-scale millennial denudation rates [Ouimet et al.,  
249 2009; Godard et al., 2010; Ansberque et al., 2015] and refer to a data set of bedrock  
250 cooling ages and corresponding exhumation rates across the mountain range from  
251 low-temperature thermochronology studies (apatite fission track (AFT), apatite  
252 (U-Th)/He (AHe), zircon fission track (ZFT) and zircon (U-Th)/He (ZHe)), compiled  
253 by Tian et al. (2013) [data from Arne et al., 1997; Kirby et al., 2002; Richardson et al.,  
254 2008; Godard et al., 2009; Wang et al., 2012; Tian et al., 2013]. Tian et al. (2013)  
255 converted the cooling ages to time-averaged exhumation rates assuming a  
256 one-dimensional, steady state upper crustal section and taking into account the effects  
257 of cooling rate on closure temperature together with heat advection during  
258 exhumation, following Reiners and Brandon (2006). For geothermal gradient, Tian et  
259 al. (2013) assumed a pre-exhumation geothermal gradient of  $20 \text{ }^\circ\text{C km}^{-1}$ , which yields  
260 a syn-exhumation gradient of  $23\text{-}30 \text{ }^\circ\text{C km}^{-1}$ , consistent with the present geothermal  
261 gradient in the Longmen Shan determined from thermal logging of local boreholes ( $>$   
262  $4.5$  km deep) and numerical modeling [Tian et al., 2013]. Uncertainties on the  
263 exhumation rates were propagated from uncertainties on thermochronology  
264 measurements [Tian et al., 2013].

265

### 266 **3.6. Calculation of seismic erosion rate over multiple earthquake cycles**

#### 267 **3.6.1. Approach to calculating seismic erosion rate**

268 Over multiple recurrence cycles, earthquakes of various magnitudes occur at different  
269 frequency. To characterize the cumulative effect, we defined a seismic erosion rate  
270 ( $\text{mm yr}^{-1}$ ) as the total volume of landslides triggered over multiple earthquake cycles  
271 and over a specified area, following Keefer (1994):

272

$$\dot{e} = \frac{\sum_{M_w} N(M_w) \times V_L(M_w)}{t \times A} \quad (1)$$

273  
274  
275 where  $t$  represents the total time (yr) over which repeated earthquakes are integrated,  
276  $A$  is the area of the region of landslide occurrence,  $N(M_w)$  is the number of  
277 landslide-triggering earthquakes in the magnitude bin  $[M_w, M_w+0.1]$ , and  $V_L(M_w)$   
278 refers the corresponding landslide volume triggered by an earthquake of magnitude  
279  $M_w$ .

280  
281 Based on the Wenchuan landslide data, we assumed that all landslides have occurred  
282 within an intensive erosion zone along the frontal Longmen Shan (Section 4.1), with  
283 an area of 170 km × 80 km ( $A$ ). This area, to first order, matches the areal extent of  
284 landslide occurrence predicted for a  $M_w$  8 event by Keefer (1994), and the length of  
285 this region also approximates the rupture length of the Wenchuan earthquake  
286 [Burchfiel et al., 2008]. By distributing the total volume of earthquake-triggered  
287 landslides over area  $A$  and time period  $t$ , we obtain a spatially and temporally  
288 averaged rate of seismic erosion.

289  
290 To calculate a seismic erosion rate from Eq. 1, we adopted a numerical integration  
291 approach (after Keefer, 1994; see details in Supporting Information). This approach  
292 combines (1) a scaling relationship between earthquake magnitude and the volume of  
293 earthquake-triggered landslides (Section 3.6.2) and (2) a statistical description of  
294 earthquake magnitude and corresponding frequency throughout an earthquake  
295 sequence (Section 3.6.3). Summing the landslide volumes throughout a full  
296 earthquake sequence, we determined the total volume of landslides occurring over a  
297 time period  $t$  that captures multiple earthquake cycles, yielding a long-term seismic  
298 erosion rate (Eq. 1).

299  
300 **3.6.2. Earthquake magnitude-landslide volume scaling relations: predictive**  
301 **models of the total volume of earthquake-triggered landslides**  
302 Descriptions of the landslide volume associated with earthquakes range from simple  
303 empirical regression of volume versus earthquake magnitude [e.g., Keefer, 1994;  
304 Malamud et al., 2004] to models that seek to capture the mechanics of landslide  
305 triggering, including slope stability as it relates to hillslope angles and near-surface  
306 rock strength [e.g., Gallen et al., 2015; Marc et al., 2016b]. Large uncertainties plague  
307 the empirical regressions, whereas the more mechanistic models – although able to  
308 reproduce global patterns [e.g., Marc et al., 2016b] – include parameters that are often  
309 not precisely known, for example those describing rock strength, earthquake asperity  
310 depth, and ground motion attenuation. To capture this range of approaches, we  
311 estimated seismic erosion rates using both empirical regression and the model of Marc  
312 et al. (2016b). We also calculated rates with a Longmen Shan-specific landslide  
313 volume model based on locally-calibrated parameters and ground motion equations.  
314 To most accurately estimate seismic erosion rates for the Longmen Shan region, we



315 evaluated the predictions of these different models with reference to the observed  
316 landslide volumes from the Wenchuan and Lushan cases (see Section 5.1). The global  
317 empirical regression model, global seismologically-based model, and Longmen  
318 Shan-specific model are summarized as follows.

319

320 **Global empirical regression:** Keefer (1994) and Malamud et al. (2004) compiled a  
321 global dataset of landslide inventories triggered by large earthquakes. They reported a  
322 logarithmic scaling relation between the total volume of landslides triggered by an  
323 earthquake,  $V_L$ , and earthquake magnitude,  $M_w$  [Malamud et al., 2004]:

324

$$325 \quad \text{Log}_{10}V_L = 1.42M_w - 11.26 (\pm 0.52) \quad (2)$$

326

327 **Global seismologically-based landslide model:** Marc et al. (2016b) developed an  
328 approach to predict the total volume of earthquake-triggered landslides, taking into  
329 account seismogenic characteristics (e.g., seismic moment and asperity depth),  
330 landscape steepness, and material sensitivity (rock strength and pore pressure). We  
331 adopted this model using seismogenic and topographic parameters appropriate for the  
332 Wenchuan and Lushan earthquakes (see discussion in Section 4.3.1 and more details  
333 in Supporting Information).

334

335 **Longmen Shan-specific landslide model:** Using local observations of ground motion  
336 attenuation, we derived an earthquake magnitude-landslide volume scaling relation  
337 specific for the Longmen Shan (details in Supporting Information). In brief, we first  
338 defined a landslide volume-PGA relation using the Wenchuan data (following  
339 Meunier et al., 2007; Figure S3a in Supporting Information). We combined this with a  
340 locally-calibrated equation describing ground motion attenuation in the Longmen  
341 Shan and neighboring areas [Cui et al., 2012; Wang et al., 2015b; and references  
342 therein]:

343

$$344 \quad \text{Log}_{10}\text{PGA} = c_1 + c_2M_w + c_3\text{Log}_{10}(D + c_4) \quad (3)$$

345

346 where  $D$  represents distance to fault trace and  $c_1$ ,  $c_2$ ,  $c_3$  and  $c_4$  are empirical  
347 parameters, determined empirically from the Wenchuan data and other earthquakes in  
348 the Longmen Shan and neighboring region (see Figure S3b in Supporting  
349 Information). Combining the landslide volume-PGA relation and the PGA- $M_w$  relation  
350 allows us to calculate the landslide volume for earthquakes across a range of  
351 earthquake magnitudes. The relation between earthquake magnitude and landslide  
352 volume can be well described by a logarithmic fit ( $r^2 = 0.99$ ):

353

$$354 \quad \text{Log}_{10}V_L = 23.77\text{Log}_{10}M_w - 11.91(\pm 0.07) \quad (4)$$

355

356 Slope angles also influence where landslides occur during earthquakes [Gallen et al.,  
357 2015; Marc et al., 2016b]. The Newmark model framework adopted by Gallen et al.  
358 (2015) accounts for slope angles but depends on assumptions about landslide

359 geometry, complicating its application in this case. However, consistent with studies  
360 of other earthquakes [Meunier et al., 2007], we find that in the case of the Longmen  
361 Shan PGA provides a good first-order empirical prediction of regional patterns in  
362 landslide occurrence without considering differences in slope angle (Figure S3a),  
363 perhaps because regional variability in slopes is relatively small when compared to  
364 PGA (Figure 1).

365

### 366 **3.6.3. Longmen Shan earthquake sequence**

367 Inferring a long-term seismic erosion rate from landslide volume predictions requires  
368 assumptions about the earthquake population over the timescales of multiple  
369 earthquake cycles. We simulated a sequence of earthquakes with various magnitudes  
370 using available seismological data from the Longmen Shan region. Because the  
371 Wenchuan earthquake ruptured almost the full length of the Longmen Shan frontal  
372 fault system [Burchfiel et al., 2008],  $M_w \sim 8$  represents a reasonable upper bound for  
373 earthquake magnitudes in the study area. We chose  $M_w \sim 5$  as a minimum magnitude  
374 for landslide triggering [Marc et al., 2016b]. The occurrence times of earthquakes of  
375 various magnitudes were determined using an earthquake frequency-magnitude  
376 distribution, with reference to regional historic seismicity data (China Earthquake  
377 Networks Center, 1657-2013) [Wang et al., 2015b] and results from  
378 paleoseismological and geodetic studies that suggest a recurrence interval (T) for  
379 Wenchuan-like events of 500 to 4000 years [Densmore et al., 2007; Shen et al., 2009;  
380 Thompson et al., 2015]. Across this range, the frequency-magnitude distribution of  
381 the Longmen Shan earthquakes could be well described using a truncated G-R  
382 function [Utsu, 1999 and references therein]. For the shortest estimated T ( $\sim 500$  years)  
383 [Thompson et al., 2015], Longmen Shan earthquake occurrence follows a classical,  
384 linear G-R relation.

385

386 To estimate seismic erosion rates following Eq. 1, we integrated predictions of the  
387 landslide volumes across the simulated earthquake sequences. Predicted landslide  
388 volumes are sensitive to the source depth of each simulated earthquake (see details in  
389 Supporting Information). For the global seismologically-based model [Marc et al.,  
390 2016b], we assumed a scaling relation between earthquake magnitude and focal depth,  
391 calibrated using the Wenchuan and the Lushan data. For the Longmen Shan-specific  
392 model, we used the scaling between earthquake magnitude and focal depth to define a  
393 characteristic landslide-triggering depth for each earthquake magnitude. We assumed  
394 that only earthquakes shallower than this depth cause landslides. For a given  
395 magnitude, we estimated the proportion of events with a focal depth shallower than  
396 this threshold based on a local seismic catalog [CSN Catalog, 2015; see Figure S4].

397

### 398 **3.6.4. Failure and resetting of hillslopes over earthquake cycles**

399 In using scaling relationships to calculate seismic erosion rate over multiple  
400 earthquake cycles, we have assumed that for each event there are sufficient hillslopes  
401 that are prone to fail. Following one earthquake cycle, failed hillslopes need to be  
402 re-weakened and re-steepened to initiate new landsliding in the following earthquake

403 cycle. We estimate that for the Longmen Shan, the pace of hillslope resetting is  
404 capable of keeping up with earthquake recurrence. For example, if we assume that the  
405 landscape fails following a patchwork fashion, then each earthquake triggers  
406 landslides on a different part of the unfailed landscape, allowing the failed hillslopes  
407 time to recover [e.g., Parker et al., 2015]. During the Wenchuan earthquake, around 1%  
408 of the high PGA-area ( $>0.2$  g) was impacted by landsliding [Li et al., 2014]. Thus to  
409 fail the full landsliding-susceptible landscape would take  $\sim 100$  earthquake cycles, or  
410 50-400 kyr (given an estimated return time of Wenchuan-like events of  $\sim 500$ -4000  
411 yrs, see Section 3.6.3). If landscapes are steepened by river incision, the steepness  
412 resetting time (i.e., time required for resetting the failed landscape to pre-Wenchuan  
413 steepness) can be approximated as the ratio of the landslide depth versus the channel  
414 incision rate. We estimate an average steepness resetting time of  $\sim 6$ -26 kyr, or  $\sim 2$ -50  
415 earthquake cycles for the Longmen Shan region (based on a mean Wenchuan  
416 landslide depth of  $\sim 6$ -13 m [Gallen et al., 2015] and a regional incision rate of  $\sim 0.5$ -1  
417  $\text{mm yr}^{-1}$  [Tian et al., 2015 and references therein]). This resetting time is much shorter  
418 than the 50-400 kyr to fully fail the landscape. Similarly, for a Longmen Shan  
419 chemical denudation rate of  $\sim 0.1$ -0.2  $\text{mm yr}^{-1}$  [Liu-Zeng et al., 2011, and references  
420 therein] we anticipate that re-weakening of hillslope material to a depth of  $\sim 6$ -13 m  
421 would take 30-130 kyr. Therefore, regional channel incision and chemical weathering  
422 propagation rates should be fast enough to re-steepen and re-weaken failed landscapes,  
423 rejuvenating hillslopes for landsliding over multiple earthquake cycles.

424

## 425 **4. Results and Discussion**

### 426 **4.1. Intensive and persistent denudation along the frontal Longmen Shan across** 427 **timescales, and its relation to seismically triggered landsliding**

#### 428 **4.1.1. Zone of focused denudation**

429 Profiles of short-term denudation rates calculated from hydrological gauging and  
430 longer-term denudation rates from cosmogenic nuclides and thermochronology are  
431 shown in Figures 1 and 2, respectively. Rates are highest along the eastern Longmen  
432 Shan front and decrease towards the Tibetan Plateau along the A-A' trend. Based on  
433 these observations, we delineate an 80 km-wide zone of intensive erosion  
434 perpendicular to the strike of the mountain range (bounded by dashed blue lines in  
435 Figure 1c). This distinct zone features steep topography, maximum PGA, and the  
436 highest concentration of Wenchuan-triggered landslides (Figure 1c and Figure 1e).  
437 This region of intensive denudation was also identified by Liu-Zeng et al. (2011)  
438 based on denudation rates calculated from 1960s-1980s hydrological gauging data,  
439 though their rates were slightly higher (up to 0.5-0.8  $\text{mm yr}^{-1}$ ) than our pre-Wenchuan  
440 (2006-2007) estimates ( $0.24 \pm 0.04$   $\text{mm yr}^{-1}$ ). The difference is consistent with  
441 background declines in both water discharge and sediment flux in the Yangtze basin  
442 over the past 50 years, attributed in part to decreased precipitation as well as to human  
443 activities like dam building [Yang et al., 2015].

444

445 Long-term denudation rates (Section 3.5) along the A-A' trend (Figure 2a, b, c, d and  
446 e) are also higher ( $> 0.5$   $\text{mm yr}^{-1}$ ) along the front of the eastern Longmen Shan,

447 compared to the western (plateau) side. The similarity to sediment flux-derived rates  
448 suggests a persistent denudation pattern across both modern and longer-term  
449 timescales. Both patterns are, to first order, similar to the distribution of the Wenchuan  
450 co-seismic landslides (Figure 2b, c, d and e). We suggest that seismicity associated  
451 with the Longmen Shan fault system, which runs along the front of the range,  
452 provides a mechanism for generating repeated landslides in this zone, as seen during  
453 the Wenchuan earthquake. The spatial coincidence of these landslides with measured  
454 denudation rates is consistent with landslides sustaining denudation fluxes across a  
455 wide range of timescales.

456

457 Additional second-order features in the exhumation data from the Longmen Shan  
458 include two local high rates to the west (Figure 2e), beyond the region of most active  
459 landsliding associated with the Wenchuan earthquake. The extent to which these high  
460 rates are also explained by earthquake-triggered landsliding is unclear, but some  
461 evidence suggests that they might be. The high exhumation rates around 160 km  
462 distance along the A-A' transect (Figure 2e) are located along the Wenchuan-Maowen  
463 fault (WMF, Figure 2f), another major thrust fault within the Longmen Shan. Rapid  
464 exhumation in this region has been attributed to active thrusting of the WMF in the  
465 late Cenozoic [Tian et al., 2013 and references therein]. Accompanying seismic  
466 activity could have triggered earthquake-triggered landsliding, converting uplifted  
467 mass to clastic sediment, enhancing denudation fluxes, and leaving imprints in the  
468 exhumation rates seen today. The other zone of locally elevated rates, closer to the  
469 plateau (Figure 2e), is less well-defined: moderately high values are recorded by the  
470 cosmogenic nuclides and seen in part of the AFT data from Arne et al. (1997) but not  
471 in other data (e.g., ZFT). A potential local maximum in denudation rate coincides with  
472 a local peak of seismic moment release (Figure 2f, A-A' distance around 200 km) as  
473 calculated from short-term historic seismicity (1970-2015) [CSN Catalog, 2015].  
474 Local clustering of seismicity might indicate the potential for landslide-triggering  
475 earthquakes in this region. Further low-temperature thermochronology would help to  
476 better constrain the exhumation pattern across the Longmen Shan and the linkage  
477 between exhumation and co-seismic landsliding.

478

#### 479 **4.1.2. Seismic control on focused denudation of the Longmen Shan**

480 In addition to seismicity, several other features also vary along the profiles shown in  
481 Figures 1 and 2, potentially influencing spatial patterns of denudation [e.g., Burbank  
482 et al., 2003; Ouimet et al., 2009]. To distinguish these effects, we have examined the  
483 relationships between denudation rates inferred from post-earthquake gauging data  
484 (2008-2012) and a group of metrics of topography (slope, relief), hydrology (mean  
485 annual runoff, proportion of runoff from high intensity runoff events), fluvial erosion  
486 potential (stream power and normalized channel steepness index), seismic shaking  
487 (PGA, distance to fault rupture as a metric for seismic energy release), and the density  
488 of earthquake-triggered landslides (Figures 3 and 4). Using principle component  
489 analysis (PCA), these metrics cluster into two statistically distinct groups that reflect  
490 mechanistically distinct processes: (1) a “seismic component”, comprising PGA,

491 landslide volumetric density and distance to fault rupture; and (2) a “non-seismic  
492 component,” comprising slope angles, relief, steepness index, and the hydrological  
493 metrics (for detailed PCA results, see Figure S5, Table S4 and Table S5 and text in  
494 Supporting Information).

495

496 Across the non-seismic metrics, post-Wenchuan denudation rates correlate positively  
497 but moderately ( $r^2 = 0.36$ ,  $P < 0.05$ , Figure 3a) with the proportion of catchment  
498 runoff from high intensity runoff events ( $> 6 \text{ mm day}^{-1}$ ), consistent with the findings  
499 of Wang et al. [2015a]. Pre-Wenchuan denudation rates also show a moderate,  
500 positive correlation with intense runoff events ( $r^2 = 0.33$ ,  $P < 0.05$ , Figure 3a), but  
501 with a shallower slope than post-earthquake rates. The steeper slope of the  
502 post-earthquake data indicates that the denudation rate has become more sensitive to  
503 hydrological conditions under enhanced sediment supply following the earthquake.  
504 We find no correlation between denudation rates and mean annual catchment runoff.  
505 There are also no statistically significant correlations between the post-Wenchuan  
506 denudation rates and other non-seismic metrics including channel steepness index and  
507 stream power (Figure 3b, c, d, e and f), perhaps because landscape steepness exceeds  
508 the threshold where these relationships are easily observed [e.g., Ouimet et al., 2009].

509

510 For seismic metrics (Figure 4), we find statistically significant correlations between  
511 post-Wenchuan denudation rates and catchment-scale mean PGA ( $r^2 = 0.61$ ,  $p < 0.002$ ,  
512 Figure 4a), catchment-scale maximum PGA ( $r^2 = 0.64$ ,  $p < 0.001$ , Figure 4b), distance  
513 to the fault rupture ( $r^2 = 0.67$ ,  $p < 0.001$ , Figure 4c), and the volumetric density of  
514 earthquake-triggered landslides ( $r^2 = 0.66$ ,  $p < 0.01$ , Figure 4d). Although USGS  
515 ShakeMap PGA data do not include local site effects and topographic amplification  
516 that may affect landslide occurrence, we expect these to have limited influence on the  
517 first-order spatial patterns that indicate a seismic control on denudation rates.

518

519 Since the principal component analysis separates these seismic parameters from the  
520 non-seismic metrics, we do not expect cross-correlation between these two groups  
521 (e.g., between PGA and catchment slope or runoff, Figure S6) to bias our  
522 interpretations. Seismic intensity and denudation rates co-vary both across the plateau  
523 margin (i.e., along A-A'), and also along strike of the range. While the former gradient  
524 coincides to some extent with changes in relief, slope, and runoff, the latter does not,  
525 emphasizing the seismic role in denudation.

526

527 The spatial coverage of the longer-term denudation rate data is not sufficient to  
528 conduct a similar analysis, but the correlations described here show that seismicity in  
529 the Longmen Shan is not inextricably coupled to other parameters that influence  
530 denudation rates. The correlation between sediment flux-derived denudation rates and  
531 seismic parameters suggests that the coincidence of high denudation rates and  
532 intensive landsliding along the frontal Longmen Shan reflects a seismic driver of  
533 denudation, rather than a coincidental relationship with an underlying control by  
534 topographic or other non-seismic parameters. We expect that the seismic control on

535 post-earthquake denudation rates as observed via sediment fluxes would recur for  
536 repeated earthquakes, providing a mechanism for seismicity to influence the  
537 longer-term pattern and rate of denudation.

538

539 We next consider the theoretical magnitude of denudation rate sustained by  
540 earthquake-triggered landsliding over multiple earthquake cycles (Section 4.2). We  
541 then compare these estimated rates of seismic erosion with the rates measured across  
542 timescales (Section 4.3).

543

## 544 **4.2. Quantifying seismic erosion rates**

### 545 **4.2.1. Predictions of landslide volumes**

546 Calculating a seismic erosion rate following Eq. 1 depends on predicting landslide  
547 volumes associated with earthquakes of varying magnitude. In Figure 5, we show  
548 results from the three predictive landslide volume models considered here: the global  
549 empirical regression of Malamud et al. (2004), the global seismologically-based  
550 model of Marc et al. (2016b), and the Longmen Shan-specific model. We compare  
551 these predictions to the volumes of landslides triggered by the Wenchuan and Lushan  
552 earthquakes, as determined from landslide mapping [Li et al., 2014; Xu et al., 2015].  
553 The global empirical regression systematically underestimates the volumes of the  
554 Wenchuan and the Lushan landslides (Figure 5a). The Longmen Shan model  
555 accurately predicts both the Wenchuan and the Lushan landslide volumes (Figure 5b).  
556 The global seismologically-based model of Marc et al. (2016b) fits the observations if  
557 adjustable parameters in the model are tuned (Figures 5c,d).

558

559 In more detail, the results of the global model of Marc et al. (2016b) are sensitive to  
560 the adopted parameters, including landscape steepness, mean asperity depth and  
561 hillslope material sensitivity. Whereas slope and asperity depth can be determined  
562 from DEM and seismological data, respectively, we lack independent constraints on  
563 the term describing material sensitivity, which is related to rock strength and pore  
564 pressure. Using a global average material sensitivity (as reported by Marc et al.,  
565 2016b) and local parameters describing seismology and topography, this model  
566 under-predicts the landslide volumes for both the Wenchuan and the Lushan  
567 earthquakes (Figure 5c). The model fits the Wenchuan and the Lushan observations  
568 for increases in the material sensitivity term of 6 times and 4.3 times, respectively.  
569 Model results for a  $5\times$  increase in material sensitivity (determined by the  
570 minimization of the sum of the squared residuals) closely approximate both volumes  
571 (Figure 5d).

572

573 Differences in curvature between the two seismologically-based  $V_L-M_w$  relations  
574 (Figure 5b vs. 5d) derive from assumptions about ground motion attenuation and the  
575 landslide volume-ground motion scaling relation. Marc et al. (2016b) assumed (i) a  
576 linear relationship between landslide volume and ground motion, in contrast to the  
577 non-linear relationship from Wenchuan-specific observations (Figure S3), and (ii) a  
578 significant “saturation” effect of ground motion at high earthquake magnitude,

579 thought to describe attenuation of high-frequency (e.g., 1 Hz) spectral accelerations  
580 [e.g., Boore and Atkinson, 2008]. Thus the Marc et al. (2016b) model predicts that  
581 ground motion and landslide volumes should increase only slightly with magnitude  
582 for large ( $M_w > \sim 6.5$ ) earthquakes. Since the magnitude dependence is small, a  $\sim 5$  km  
583 shallower asperity depth is needed in this model to explain the much greater landslide  
584 volume from the Wenchuan earthquake ( $M_w=7.9$ ;  $V_L=2.7-4.4$  km<sup>3</sup>) vs. the Lushan  
585 event ( $M_w=6.6$ ;  $V_L=0.042$  km<sup>3</sup> from Xu et al., 2015, although Marc et al., 2016b  
586 quoted a lower volume for this event), assuming similar material sensitivity.

587

#### 588 **4.2.2. Seismic erosion rates**

589 The Longmen Shan earthquake frequency-magnitude distribution depends on the  
590 recurrence interval for Wenchuan-like events,  $T$  (Section 3.6.3, Figure 6a); across the  
591 range of plausible estimates for  $T$  ( $\sim 500-4000$  years), we find a lower seismic erosion  
592 rate with longer  $T$  (Figure 5b). For a given  $T$ , the corresponding seismic erosion rate  
593 also differs depending on the landslide volume model (Figure S7). Using the  
594 Longmen Shan seismologically-based landslide volume model (Figure 5b), we  
595 calculate an erosion rate of  $0.44-0.96$  mm yr<sup>-1</sup> (with a central estimate of  $0.51-0.81$   
596 mm yr<sup>-1</sup>), which reduces to  $0.34-0.81$  mm yr<sup>-1</sup> (with a central estimate of  $0.40-0.69$   
597 mm yr<sup>-1</sup>) taking into account focal depth (Figure 6b). The rates calculated using the  
598 global empirical regression [Keefer, 1994] and the global seismologically-based  
599 model [Marc et al., 2016b] are lower than the result using our Longmen Shan-specific  
600 model. This outcome is not surprising, since the two former models underestimate the  
601 observed landslide volumes for Wenchuan and Lushan, a discrepancy that we attribute  
602 to uncertainties in applying globally-calibrated parameters to a specific region (see  
603 Section 4.3.1, above). On the other hand, using the global seismologically-based  
604 model with the  $\sim 5\times$  increase in material sensitivity that captures the observed  
605 Longman Shan volumes (Figure 5d) yields a seismic erosion rate of  $0.37-1.68$  mm  
606 yr<sup>-1</sup>, with a central estimate of  $0.73-0.99$  mm yr<sup>-1</sup>, close to that calculated from the  
607 Longmen Shan-specific model although slightly higher because of the strong  
608 non-linearity of the global model. These comparisons emphasize the sensitivity of  
609 landslide erosion calculations to model assumptions, and particularly the importance  
610 of using locally calibrated parameters since global average values may not accurately  
611 reflect a specific region (as suggested by Keefer, 1994).

612

### 613 **4.3. Comparing magnitudes of denudation rates across different timescales**

#### 614 **4.3.1. Average denudation rate of the frontal Longmen Shan**

615 The catchment area-weighted means ( $\pm 1$  standard deviation) of pre-Wenchuan and  
616 post-Wenchuan denudation rates inferred from hydrological gauging are  $0.24 \pm 0.04$   
617 mm yr<sup>-1</sup> and  $1.09 \pm 0.13$  mm yr<sup>-1</sup> respectively. The equivalent average kyr-timescale  
618 cosmogenic nuclide-derived denudation rate is  $0.55 \pm 0.05$  mm yr<sup>-1</sup>. For denudation  
619 over Myr timescales, we interpolate the exhumation rates in the intensive erosion  
620 zone and run 1,000,000 Monte Carlo random simulations to account for the  
621 uncertainties from individual exhumation rate estimates. The resulting Myr  
622 denudation rate is  $0.61+0.14/-0.08$  mm yr<sup>-1</sup> (uncertainties indicate the 16<sup>th</sup> and 84<sup>th</sup>

623 percentiles of the Monte Carlo results). The inferred seismic erosion rates over  
624 multiple earthquake cycles range from 0.34 to 0.81 mm yr<sup>-1</sup> across the range of  
625 plausible T values (500-4000 years), using the Longmen Shan-specific  
626 seismologically-based  $V_L$ - $M_w$  relation.

627

#### 628 **4.3.2. Pre- and Post-Wenchuan earthquake sediment fluxes versus long-term** 629 **denudation rate**

630 The 2006-2007 pre-Wenchuan denudation rate calculated from sediment fluxes is  
631 lower than the long-term denudation rate. The rate reported from the 1960s to 1980s  
632 gauging data is higher than that calculated from the 2006-2007 data, but still slightly  
633 lower than the long-term rate. In contrast, the post-Wenchuan sediment flux-derived  
634 denudation rate is the highest amongst all observed denudation rates (Figure 7). The  
635 long-term average denudation rates (i.e., from cosmogenics and thermochronology)  
636 thus fall between the immediate pre- and post-earthquake values derived from  
637 sediment fluxes. In general terms, this pattern is consistent with a conceptual model  
638 for erosional dynamics over one complete earthquake cycle in which the  
639 pre-earthquake rates reflect below-average values and the post-earthquake rates  
640 reflect an immediate post-seismic denudational pulse [Ouimet, 2010]. However, given  
641 the large variability in pre-earthquake rates (comparing 2006-2007 data vs.  
642 1960s-1980s), it is difficult to use these data to evaluate quantitatively the extent to  
643 which the post-earthquake pulse contributes to the long-term budget; considering the  
644 2006-2007 data alone, the post-earthquake pulse would need to play a major role to  
645 make the long-term value, but considering the data from the 1960s-1980s, this role  
646 would need to be relatively small over the long term.

647

#### 648 **4.3.3. Seismic erosion rate vs. long-term denudation rate**

649 Our best estimate of the seismic erosion rate (0.34-0.81 mm yr<sup>-1</sup>, using the Longmen  
650 Shan-specific landslide volume model) is comparable to the measured long-term  
651 denudation rates of the frontal Longmen Shan (kyr denudation rate: 0.55 ± 0.05 mm  
652 yr<sup>-1</sup>; Myr exhumation rate: 0.61 ± 0.14 / -0.08 mm yr<sup>-1</sup>) (Figure 7). Using the global  
653 seismologically-based model for landslide volumes yields a slightly higher calculated  
654 denudation rate via earthquake-induced landslides (0.37-1.68 mm yr<sup>-1</sup>, with central  
655 estimate of 0.73-0.99 mm yr<sup>-1</sup>; Figure S7). Denudation rates determined either from  
656 gauging data and long-term chronometers include mass loss via dissolved load in  
657 addition to via physical erosion. If dissolved load is mainly derived from weathering  
658 of landslide material [e.g., Emberson et al., 2016], the calculated seismic erosion rate  
659 should be directly comparable to the denudation rate. Significant non-landslide solute  
660 sources, such as from ground water release [e.g., Jin et al., 2016], would increase the  
661 denudation rate compared to the calculated seismic erosion rates, although such  
662 effects should be small since dissolved load represents a relatively low proportion of  
663 the total denudation flux (~20%, Section 3.4). Either way, additional dissolved load  
664 contributions would not explain a lower measured denudation rate compared to the  
665 calculated seismic erosion rate.

666



667 We recognize that not all landslide material is necessarily evacuated from a mountain  
668 belt by rivers within one earthquake cycle. Landslide erosion rates could be higher  
669 than actual measured long-term denudation rates if new seismically triggered  
670 landslides re-mobilize debris associated with prior earthquakes. Given the relatively  
671 rapid rates of sediment evacuation observed in the Longmen Shan region compared to  
672 the long earthquake recurrence times [Liu et al., 2013] and the lack of extensive  
673 storage of intra-montane landslide debris in this setting [Parker et al., 2011], we view  
674 near-complete evacuation as a reasonable first-order assumption for comparing rates.  
675 If this is the case, the seismic erosion rates calculated from the Longmen  
676 Shan-specific landslide volume model are consistent with the measured long-term  
677 denudation rates.

678  
679 Whether the seismic erosion rate is similar in magnitude or slightly higher than the  
680 measured long-term rate (Figure 7), our results demonstrate that, at least in this region,  
681 earthquake-triggered landslides are capable of sustaining denudation rates that are  
682 comparable to long-term averages at the mountain belt scale and over timescales of  
683 multiple seismic cycles. A corollary is that the observed erosional fluxes are likely to  
684 be dominated by material derived from earthquake-triggered landslides, with  
685 implications not only for sediment dynamics and landscape evolution, but also for  
686 biogeochemical cycles [e.g., Jin et al., 2016; Emberson et al., 2016].

687  
688 Over longer timescales, climate fluctuations may influence the capacity of the  
689 sediment routing systems for removing landslide debris and maintaining river incision  
690 and hillslope weathering rates required to sustain landslides. Indeed, we find that high  
691 intensity runoff events help to explain the observed short-term denudation rates in the  
692 Longmen Shan (Fig. 3a), pointing to the importance of climate variability as an  
693 erosional agent. Thus we expect that climate – which may have changed in response  
694 to topographic evolution [e.g., Molnar et al., 2010] – interacts with seismic events to  
695 influence the pace of surface processes in the Longmen Shan, even though a primary  
696 control may be related to the seismotectonic processes that trigger landslides and thus  
697 convert rocks to erodible sediment. Our results suggest that earthquake-triggered  
698 landslides can focus denudation in mountains where rivers have the capacity to  
699 transport and export the excess sediment supplied from hillslopes (e.g. Fig. 3a). In  
700 these settings the denudation can be considered as tectonically limited [Montgomery  
701 and Brandon, 2002], yet fully understanding topographic evolution will require better  
702 understanding how landslide frequency and magnitude, and the associated fluvial  
703 export of sediment, respond to long-term climatic fluctuations.

704

## 705 **5. Conclusions and Implications**

706 By considering the effects of multiple earthquakes, we calculate that co-seismic  
707 landslides can sustain denudation rates that are similar to the rates recorded by  
708 chronometers over timescales of thousands to millions of years (Figure 7). In addition  
709 to similar magnitudes, we find a first-order spatial coincidence of long-term  
710 denudation and Wenchuan-triggered landslides (Section 4.1, Figure 2), and a

711 correlation between the sediment-derived denudation rates and co-seismic landsliding  
712 (Figure 4d). Over the long term, the location of earthquake-triggered landslides  
713 should reflect earthquake sources and ground motion attenuation, with landslide  
714 density decreasing away from seismogenic faults [Meunier et al., 2007], as we also  
715 observe for the Wenchuan case.

716

717 Our observations suggest that the long-term location and rate of denudation in the  
718 Longmen Shan is consistent with the focusing of seismic energy release along  
719 range-bounding faults, with the resulting landslides serving as a primary mechanism  
720 sustaining denudation fluxes. Landslides can only continue to operate as effective  
721 denudation mechanisms if hillslopes are sufficiently steep. It is likely that the  
722 combination of uplift, river incision, and fluvial evacuation of sediment [e.g., Burbank  
723 et al., 1996; Bennett et al., 2016] is capable of continually re-steepening and  
724 re-weakening failed landscapes between earthquake cycles. Earthquakes should  
725 increase the efficiency of landslide generation for a given steepness and hillslope  
726 strength, such that the location of most intense erosion at the orogenic scale may be  
727 determined by seismic energy release. These effects could be enhanced by rock  
728 weakening resulting from greater deformation and orographic rainfall close to  
729 mountain fronts [Gallen et al., 2015; Vanmaercke et al., 2017]. We thus suggest that  
730 focused denudation along a high-relief plateau margin may be regulated at least in  
731 part by the location and activity of seismogenic faulting, and specifically by the  
732 resulting earthquake-triggered landslides.

733

### 734 **Acknowledgements**

735 This research was supported by the U.S. National Science Foundation  
736 (NSF-EAR/GLD grant 1053504 to A.J.W.) and the Chinese Academy of Sciences  
737 (YIS fellowship grant 2011Y2ZA04 to A.J.W.). G.L. was supported by the USC  
738 Dornsife College Merit Fellowship and a GSA graduate student research grant. This  
739 work benefited from conversations with Sean Gallen, Niels Hovius, Odin Marc,  
740 Haoran Meng, Joel Scheingross, James Dolan and Seulgi Moon. We thank  
741 constructive comments from an anonymous reviewer that greatly helped to improve  
742 an earlier version of the manuscript and An Yin for editorial handling.

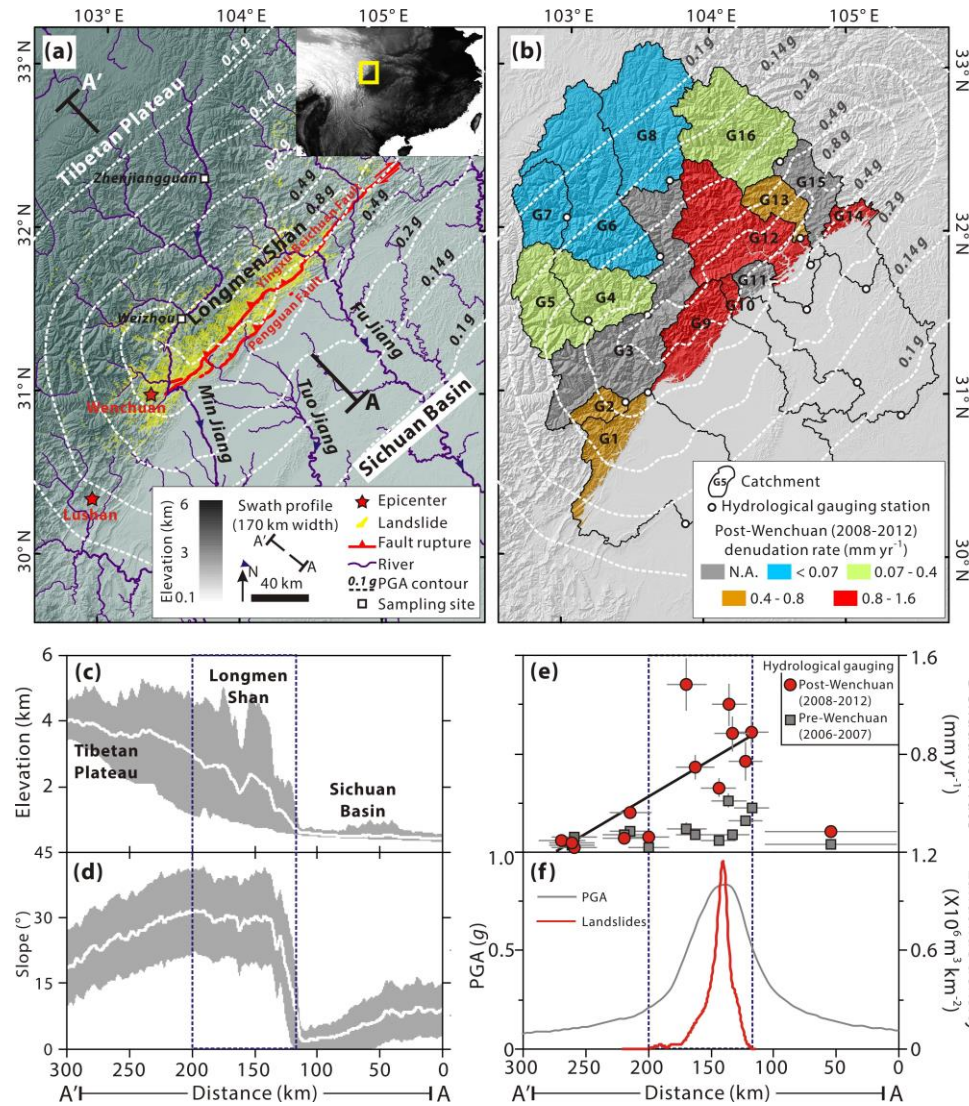
743

744

745

746  
747  
748  
749

Figure 1.



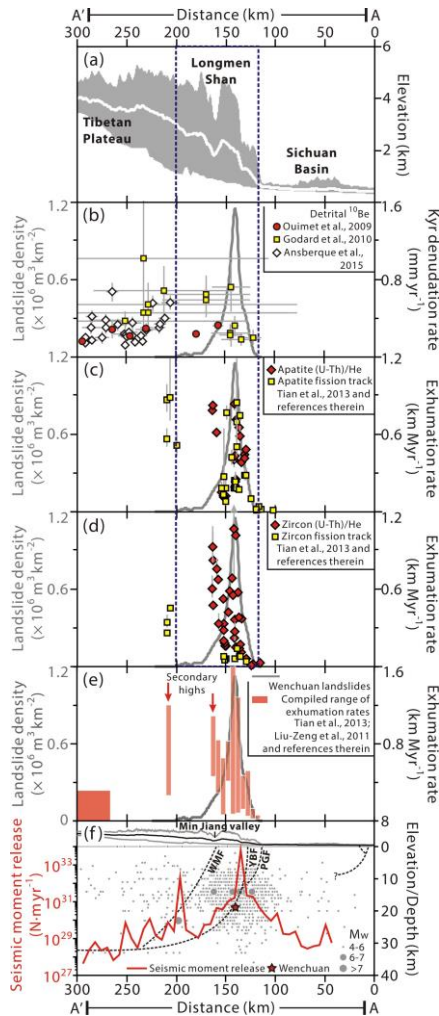
750

751 Figure 1. Maps of topography of the study area, locations of the  $M_w$ 7.9 2008  
752 Wenchuan and the  $M_w$ 6.6 2013 Lushan earthquakes, the Wenchuan peak ground  
753 accelerations (PGA) (gridded data from the USGS hazards program,  
754 <http://earthquake.usgs.gov/earthquakes>), Wenchuan-triggered landslides and  
755 post-Wenchuan gauging-derived denudation rates, and swath profiles of topography,  
756 denudation rates, PGA, and landslides. (a) Map of the  $M_w$ 7.9 2008 Wenchuan  
757 earthquake and the  $M_w$ 6.6 Lushan earthquake epicenters (red stars), mapped  
758 Wenchuan earthquake-triggered landslides (yellow polygons) over shaded relief map,  
759 Wenchuan PGA contours (dashed lines), the trend of the 170 km-wide swath profile  
760 (A-A'), sampling sites of river water samples (Jin et al., 2016) (squares), Wenchuan  
761 earthquake surface rupture (red lines), and the regional context of the study area (inset  
762 panel); (b) map of post-seismic sediment flux-derived denudation rates upstream of  
763 hydrological gauging stations (circles); denudation rates are normalized to areas with

764 elevation > 800 m to account for limited contribution from flat frontal plains; (c)  
765 swath profile of the topography projected along A-A' showing the mean (white line)  
766 and maximum and minimum elevations (grey area); blue dashed lines delimit the zone  
767 with intensive denudation between profile distances of 120 km and 200 km); (d)  
768 swath profile of slopes (°) projected along A-A' with mean slope (white line) ±1  
769 standard deviation on the mean slope (grey area); (e) swath profile of pre-Wenchuan  
770 earthquake (2006-2007, red circles) and post-Wenchuan earthquake (2008-2012, grey  
771 squares) denudation rates (y-axis error bars = ±1 s.d. uncertainties in denudation rates,  
772 x-axis error bars = square root of catchment area), the decreasing trend of  
773 post-seismic denudation rates along the swath is shown by least-squares fitting of  
774 denudation vs. distance along A-A' (solid black line); for denudation in the frontal  
775 Sichuan basin, we divide the estimated denudation fluxes by the total catchment area  
776 including areas with elevation < 800 m, and this provides an upper limit; (f) swath  
777 profiles sampled at 5 km-intervals along A-A' of PGA (grey) and the volumetric  
778 density for all landslides (red, m<sup>3</sup> km<sup>-2</sup>, landslide volume over the specified area).

779

780 Figure 2.



781

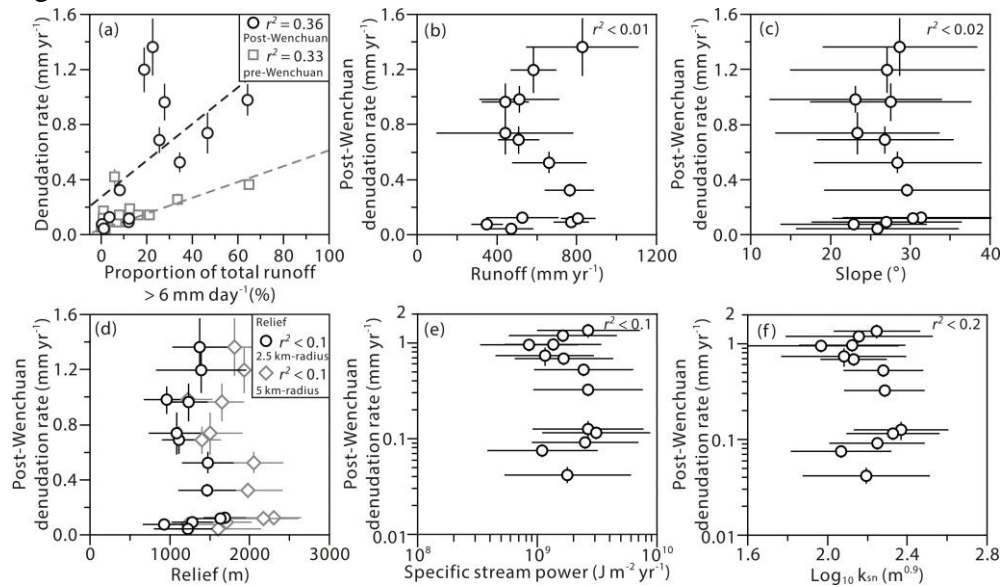
782

783 Figure 2. Swath profiles of topography, millennial denudation rates, geological  
 784 exhumation rates and seismicity across the Longmen Shan range. (a) Swath profile of  
 785 topography along the Longmen Shan range (A-A'); white line – mean elevations; grey  
 786 area – minimum-maximum elevation envelop; blue dashed lines bound the intensive  
 787 denudation zone as defined in Figure 1; (b) swath profile of  $^{10}\text{Be}$ -derived millennial  
 788 denudation rates; error bars on the y-axis indicate  $\pm 1$  s.d. uncertainties, and on the  
 789 x-axis the square roots of the catchment area; (c) swath profile of apatite fission track  
 790 (AFT) and apatite (U-Th)/He (AHe)-determined exhumation rates; error bars are  $\pm 1$   
 791 s.d. uncertainties; (d) swath profile of zircon (U-Th)/He (ZHe) and zircon fission track  
 792 (ZFT)-determined exhumation rates with  $\pm 1$  s.d. uncertainties (error bars); (e) swath  
 793 profile of compiled exhumation rates (red bars: range of exhumation rates including  
 794 uncertainties; for data with distance < 250 km, data points are binned in 5 km-wide  
 795 increments); the grey curves on (b), (c), (d) and (e) show the Wenchuan landslide  
 796 distribution, as in Figure 1f; (f) swath profiles of topography (black solid curve: mean  
 797 elevations; grey solid curves: minimum and maximum elevations), historic seismicity  
 798 (1970-2015, grey circles sized by the estimated magnitude; star: Wenchuan

799 earthquake) [CSN Catalog, 2015] and seismic moment release (red curve, data binned  
 800 in 5 km-wide increments), and a simplified sketch of the Longmen Shan fault system  
 801 (WMF: Wenchuan-Maowen fault; YBF: Yingxiu-Beichuan fault; PGF:  
 802 Pengxian-Guanxian fault) [Liu-Zeng et al., 2011; Ansberque et al., 2015 and  
 803 references therein].

804  
 805

806 Figure 3.

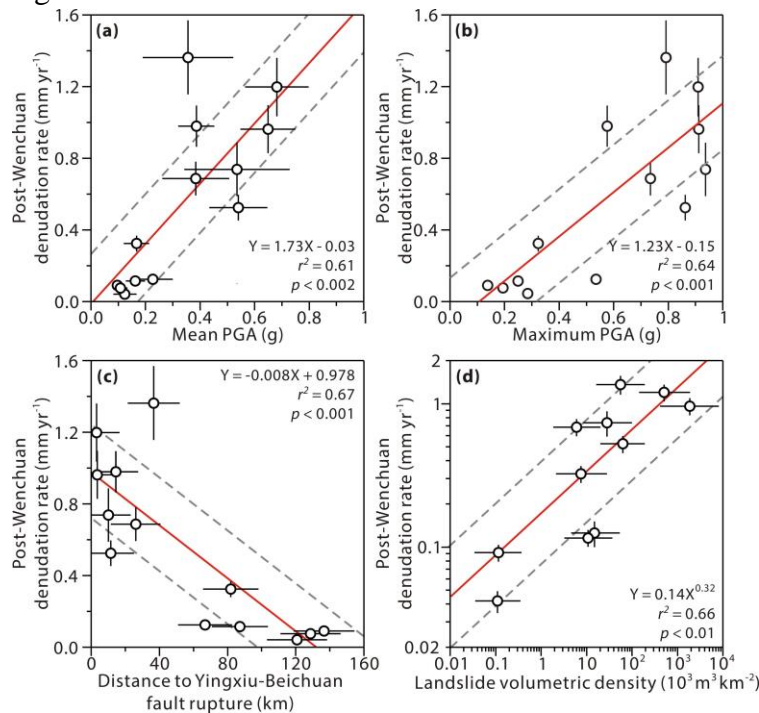


807

808 Figure 3. Sediment flux-derived denudation rates for the catchments draining the  
 809 Longmen Shan plotted versus hydrological and topographic metrics. (a),  
 810 Post-Wenchuan (circles) and pre-Wenchuan (squares) denudation rate as a function of  
 811 the proportion of total runoff from days with runoff > 6 mm day<sup>-1</sup>; post-Wenchuan  
 812 denudation rate plotted versus annual runoff (b), slope (c), and relief (d); relief is  
 813 calculated as the ranges of elevations over 2.5 km-radius (circles) and 5 km-radius  
 814 (diamonds) circular windows. (e), Post-Wenchuan denudation rate against specific  
 815 stream power calculated using the approach in Burbank et al., (2003) and Ansberque  
 816 et al. (2015). (f), Post-Wenchuan denudation rate vs. normalized channel steepness  
 817 index calculated using Stream Profiler (<http://www.geomorphtools.org>) and  
 818 normalized to  $\theta_{ref} = 0.45$ . All error bars represent  $\pm 1$  s.d. uncertainties.

819  
820  
821  
822

Figure 4.



823

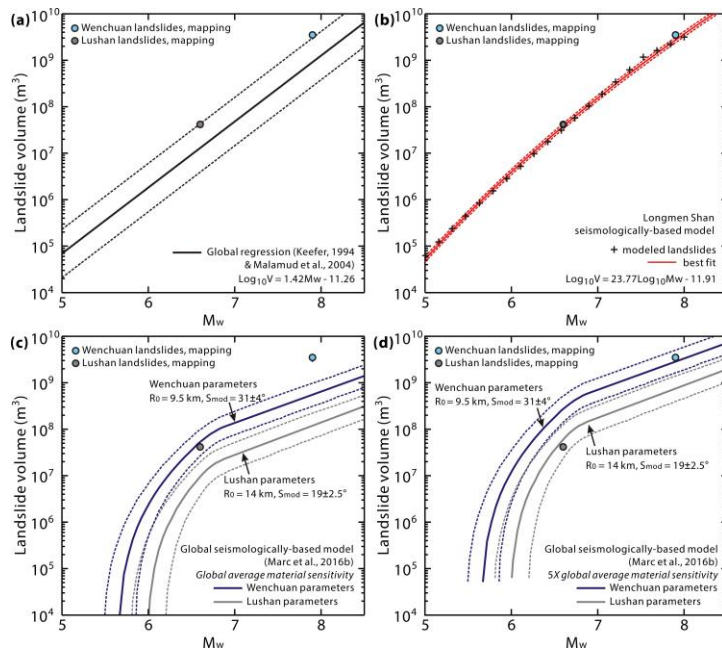
824 Figure 4. Relationships between sediment flux-derived denudation rates and seismic  
825 parameters. Post-Wenchuan denudation rate as a function of: (a) catchment mean  
826 PGA; (b) catchment maximum PGA; (c) mean distance of each catchment to the  
827 Yingxiu-Beichuan fault rupture; and (d) landslide volumetric density. Red solid lines  
828 show best fits from linear least-squares regression (performed in the logarithmic space  
829 for d); grey dashed lines show  $\pm 1$  s.d. uncertainties of the fits; error bars for  
830 denudation and PGA indicate  $\pm 1$  s.d. uncertainties; error bars for distance to the fault  
831 rupture are the square roots of catchment area; landslide volumetric densities are  
832 reported as the median values and the 16<sup>th</sup> and 84<sup>th</sup> percentiles of the distribution (i.e.,  
833 ranges of  $\pm 1$  s.d. in a standard normal distribution) from the results from 1000 Monte  
834 Carlo random sampling simulations.

835

836

837

Figure 5.



838

839 Figure 5. Earthquake-triggered landslide volume models. (a) Global empirical  
 840 regression between earthquake magnitude and associated landslide volume [Keefer,  
 841 1994; Malamud et al., 2004]; solid line represents the logarithmic least squares linear  
 842 fit; dashed lines show  $\pm 1$  s.d. uncertainties (residual errors) of the fit; the blue and the  
 843 grey circles are Wenchuan and the Lushan data, respectively; (b) Longmen  
 844 Shan-specific, seismologically-based landslide volume model; the crosses represent  
 845 the modeled landslide volumes for 20 earthquakes with magnitude from 5 to 8; the  
 846 solid curve represents the best fit of the modeled landslide volumes as a function of  
 847 earthquake magnitude (details in the Supporting Information); the dashed curves show  
 848  $\pm 1$  s.d. uncertainties (residual errors) of the fit; (c) a global seismologically-based  
 849 landslide volume model [Marc et al., 2016b]; the blue and grey curves refer to the  
 850 modeled landslide volumes using the Wenchuan parameters (mean asperity depth =  
 851 9.5 km, modal slope =  $31 \pm 4^\circ$ , uncertainty: range at 98% of modal slope frequency  
 852 defined in Marc et al., 2016b) and the Lushan parameters (mean asperity depth = 14  
 853 km, modal slope =  $19 \pm 2.5^\circ$ , uncertainty: range at 98% of modal slope frequency  
 854 defined in Marc et al., 2016b), respectively, both using global average material  
 855 sensitivity; dashed curves show 68% confidence interval from Monte Carlo  
 856 simulations accounting for uncertainties of the relevant parameters (Marc et al., 2016b;  
 857 details in Supporting Information); (d) the modeled results from the model of Marc et  
 858 al. 2016b with  $5 \times$  material sensitivity.

859

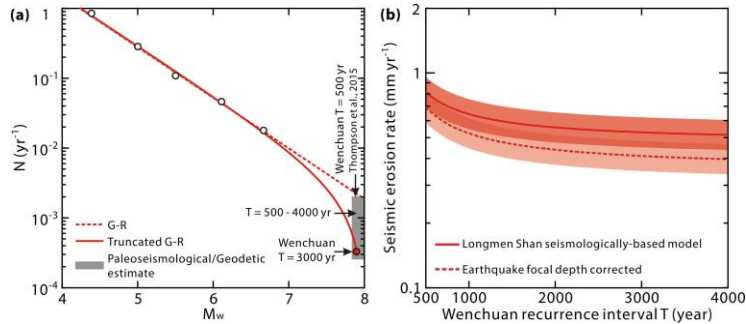


860

861

862

Figure 6.



863

864 Figure 6. Earthquake magnitude-frequency distribution of the Longmen Shan region,  
865 and the calculated seismic erosion rate. (a) Longmen Shan earthquake  
866 magnitude-frequency relation described by a truncated Gutenberg-Richter relation  
867 [Utsu, 1999] using historic seismicity data (white circles) [Wang et al., 2015b] and the  
868 recurrence interval ( $T$ ) for Wenchuan-like events from paleoseismological/geodetic  
869 studies (grey-shaded zone); red dot and solid curve – truncated G-R relation for  $T =$   
870 3000 years [Shen et al., 2009]; dashed line – linear G-R relation, which fits  $T \sim 500$   
871 years [Thompson et al., 2015]; (b) calculated seismic erosion rate with the Longmen  
872 Shan seismologically-based landslide volume model as a function of the estimated  
873 recurrence interval for Wenchuan-alike events,  $T$ ; shaded area shows  $\pm 1$  s.d; the solid  
874 curve shows results assuming landslides are triggered by all simulated earthquakes;  
875 the dashed curve includes a threshold focal depth for earthquake triggering.

876

877

878

879 Figure 7.

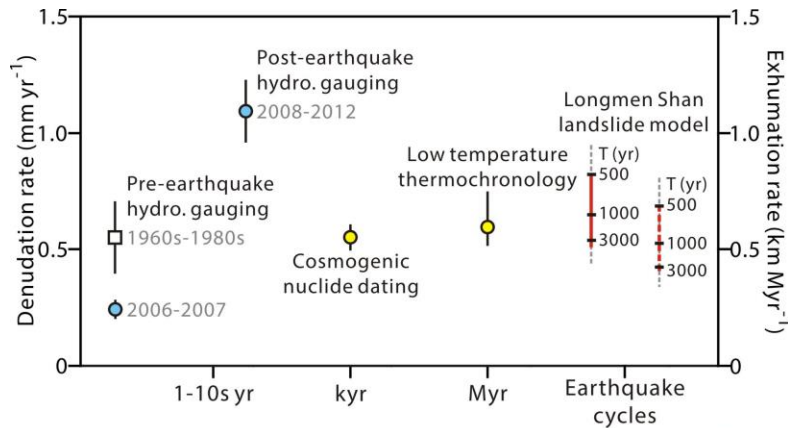


Figure 7

880

881 Figure 7. Denudation rates of the frontal Longmen Shan across different timescales.  
882 The blue circles show pre-Wenchuan and post-Wenchuan earthquake denudation rates  
883 determined from hydrological gauging; the square shows pre-Wenchuan earthquake  
884 (1960s-1980s) denudation rates reported in Liu-Zeng et al. (2011); yellow circles  
885 show long-term denudation rates determined from  $^{10}\text{Be}$  measurements and low  
886 temperature thermochronology analysis (AFT and AHe). For catchment-scale  
887 denudation (river gauging and  $^{10}\text{Be}$  studies), the denudation rates are the catchment  
888 area-weighted means, and the error bars represent catchment area-weighted 1 s.d.  
889 uncertainty. For the low temperature thermochronology-based denudation estimate,  
890 the denudation rate is reported as the average after interpolating the exhumation data  
891 compiled in Tian et al. (2013), with uncertainties propagated from the reported  
892 uncertainties in individual exhumation rate estimate [Tian et al., 2013]. Red bars with  
893 black ticks show seismic erosion rates across the range of estimated Wenchuan  
894 recurrence intervals ( $T=500-4000$  years), with a solid red bar for all earthquakes, a  
895 dashed red bar considering focal depth threshold (see Fig. 6), and black ticks for noted  
896  $T$  values; dashed grey line = 1 s.d. uncertainties.

897

898

899

900

901 Table 1. Notation for symbols

Symbol	Notation	Unit
$A$	Area of landslide occurrence over earthquake cycles	$\text{km}^2$
$c_1 c_2 c_3 c_4$	Parameters of ground motion attenuation equation, Longmen Shan	
$D$	Distance to fault rupture	km
$\dot{e}$	Seismic erosion rate	$\text{mm yr}^{-1}$
$k_{sn}$	Normalized channel steepness index	$\text{m}^{0.9}$
$M_w$	Earthquake moment magnitude	-
$N(M_w)$	Number of earthquakes in the magnitude bin $[M_w, M_w + 0.1]$	
$R_0$	Mean asperity depth	km
$S_{mod}$	Modal slope	$^\circ$
$t$	Time period of multiple earthquake cycles	yr
$T$	Recurrence interval for Wenchuan-like earthquakes	yr
$V_L$	Landslide volume	$\text{m}^3$
$\theta_{ref}$	Reference concavity index	-
$\omega$	Specific stream power	$\text{J m}^{-2}$ $\text{yr}^{-1}$

902

903

904

905

906 **References**

- 907 Ansberque, C., V. Godard, O. Bellier, J. De Sigoyer, J. Liu-Zeng, X. Xu, Z. Ren, Y. Li, and A. S. T. E.  
908 R. Team (2015), Denudation pattern across the Longriba fault system and implications for the  
909 geomorphological evolution of the eastern Tibetan margin, *Geomorphology*, 246, 542-557, doi:  
910 10.1016/j.geomorph.2015.07.017.
- 911 Arne, D., B. Worley, C. Wilson, S. F. Chen, D. Foster, Z. L. Luo, S. G. Liu, and P. Dirks (1997),  
912 Differential exhumation in response to episodic thrusting along the eastern margin of the Tibetan  
913 Plateau, *Tectonophysics*, 280(3-4), 239-256, doi: 10.1016/S0040-1951(97)00040-1.
- 914 Bennett, G. L., S. R. Miller, J. J. Roering, and D. A. Schmidt (2016), Landslides, threshold slopes, and  
915 the survival of relict terrain in the wake of the Mendocino Triple Junction, *Geology*, doi:  
916 10.1130/g37530.1.
- 917 Beaumont, C., R. A. Jamieson, M. H. Nguyen, and B. Lee (2001), Himalayan tectonics explained by  
918 extrusion of a low-viscosity crustal channel coupled to focused surface denudation, *Nature*,  
919 414(6865), 738-742, doi: 10.1038/414738a.
- 920 Burchfiel, B. C., L. H. R., R.D. van der Hilst, B.H. Hager, Z. Chen, R.W. King, C. Li, J. Lü, H. Yao,  
921 and E. Kirby (2008), A geological and geophysical context for the Wenchuan earthquake of 12 May  
922 2008, Sichuan, People's Republic of China, *GSA Today*, 18(7), 5, doi: 10.1130/GSATG18A.1.
- 923 Burbank, D. W., J. Leland, E. Fielding, R. S. Anderson, N. Brozovic, M. R. Reid, and C. Duncan  
924 (1996), Bedrock incision, rock uplift and threshold hillslopes in the northwestern Himalayas, *Nature*,  
925 379(6565), 505-510, doi:10.1038/379505a0.
- 926 Burbank, D. W., A. E. Blythe, J. Putkonen, B. Pratt-Sitaula, E. Gabet, M. Oskin, A. Barros, and T. P.  
927 Ojha (2003), Decoupling of erosion and precipitation in the Himalayas, *Nature*, 426(6967), 652-655,  
928 doi:10.1038/nature02187.
- 929 Clark, M. K., and L. H. Royden (2000), Topographic ooze: Building the eastern margin of Tibet by  
930 lower crustal flow, *Geology*, 28(8), 703-706, doi:  
931 10.1130/0091-7613(2000)28<703:tobtem>2.0.co;2.
- 932 CSN Catalog (2015), data collected by the China Seismograph Network stations, Copyrighted &  
933 produced by China Earthquake Networks Center (CENC)  
934 ([http://www.csnmc.ac.cn/wdc4seis@bj/earthquakes/csn\\_catalog\\_p001.jsp](http://www.csnmc.ac.cn/wdc4seis@bj/earthquakes/csn_catalog_p001.jsp))
- 935 Cui, J.W., J.G. Zhang, D. Gao, J.X. Duan and T. Wang (2012), The ground motion attenuation relation  
936 for the Mountainous area in Sichuan and Yunnan, 15th World Conference on Earthquake  
937 Engineering 2012, 1, 668-677.
- 938 Densmore, A. L., M. A. Ellis, Y. Li, R. J. Zhou, G. S. Hancock, and N. Richardson (2007), Active  
939 tectonics of the Beichuan and Pengguan faults at the eastern margin of the Tibetan Plateau, *Tectonics*,  
940 26(4), doi: 10.1029/2006tc001987.
- 941 Emberson, R., N. Hovius, A. Galy, and O. Marc (2016), Chemical weathering in active mountain belts  
942 controlled by stochastic bedrock landsliding, *Nature Geoscience*, 9(1), 42-45, doi:  
943 10.1038/ngeo2600.
- 944 Gallen, S. F., M. K. Clark, and J. W. Godt (2015), Coseismic landslides reveal near-surface rock  
945 strength in a high-relief, tectonically active setting, *Geology*, 43(1), 11-14, doi: 10.1130/g36080.1.
- 946 Godard, V., J. Lave, J. Carcaillet, R. Cattin, D. Bourles, and J. Zhu (2010), Spatial distribution of  
947 denudation in Eastern Tibet and regressive erosion of plateau margins, *Tectonophysics*, 491(1-4),  
948 253-274, doi: 10.1016/j.tecto.2009.10.026.

949 Godard, V., R. Pik, J. Lave, R. Cattin, B. Tibari, J. de Sigoyer, M. Pubellier, and J. Zhu (2009), Late  
950 Cenozoic evolution of the central Longmen Shan, eastern Tibet: Insight from (U-Th)/He  
951 thermochronometry, *Tectonics*, 28, TC5009, doi: 10.1029/2008tc002407.

952 Hovius, N., P. Meunier, L. Ching-Weei, C. Hongey, C. Yue-Gau, S. Dadson, H. Ming-Jame, and M.  
953 Lines (2011), Prolonged seismically induced erosion and the mass balance of a large earthquake,  
954 *Earth and Planetary Science Letters*, 304(3-4), 347-355, doi: 10.1016/j.epsl.2011.02.005.

955 Hubbard, J., and J. H. Shaw (2009), Uplift of the Longmen Shan and Tibetan plateau, and the 2008  
956 Wenchuan (M=7.9) earthquake, *Nature*, 458(7235), 194-197, doi: Doi 10.1038/Nature07837.

957 Jarvis, A., H.I. Reuter, A. Nelson, E. Guevara, 2008, Hole-filled SRTM for the globe Version 4,  
958 available from the CGIAR-CSI SRTM 90m Database (<http://srtm.csi.cgiar.org>).

959 Jin, Z., A. J. West, F. Zhang, Z. An, R. G. Hilton, J. Yu, J. Wang, G. Li, L. Deng, and X. Wang (2016),  
960 Seismically enhanced solute fluxes in the Yangtze River headwaters following the A.D. 2008  
961 Wenchuan earthquake, *Geology*, 44(1), 47-50, doi: 10.1130/g37246.1.

962 Keefer, D. K. (1994), The Importance of Earthquake-Induced Landslides to Long-Term Slope Erosion  
963 and Slope-Failure Hazards in Seismically Active Regions, *Geomorphology*, 10(1-4), 265-284, doi:  
964 10.1016/0169-555x(94)90021-3.

965 Kirby, E., P. W. Reiners, M. A. Krol, K. X. Whipple, K. V. Hodges, K. A. Farley, W. Tang, and Z. Chen  
966 (2002), Late Cenozoic evolution of the eastern margin of the Tibetan Plateau: Inferences from  
967 <sup>40</sup>Ar/<sup>39</sup>Ar and (U-Th)/He thermochronology, *Tectonics*, 21(1), doi: 10.1029/2000tc001246.

968 Larsen, I. J., D. R. Montgomery, and O. Korup (2010), Landslide erosion controlled by hillslope  
969 material, *Nature Geoscience*, 3(4), 247-251, doi: 10.1038/ngeo776.

970 Larsen, I. J., D. R. Montgomery, and H. M. Greenberg (2014), The contribution of mountains to global  
971 denudation, *Geology*, doi: 10.1130/g35136.1.

972 Lavé J., and D. Burbank (2004), Denudation processes and rates in the Transverse Ranges, southern  
973 California: Erosional response of a transitional landscape to external and anthropogenic forcing,  
974 *Journal of Geophysical Research: Earth Surface*, 109(F1), 1-31, doi: 10.1029/2003jf000023.

975 Li, G., A. J. West, A. L. Densmore, Z. Jin, R. N. Parker, and R. G. Hilton (2014), Seismic mountain  
976 building: Landslides associated with the 2008 Wenchuan earthquake in the context of a generalized  
977 model for earthquake volume balance, *Geochemistry, Geophysics, Geosystems*, 15(4), 833-844, doi:  
978 10.1002/2013gc005067.

979 Li, G., A. J. West, A. L. Densmore, D. E. Hammond, Z. Jin, F. Zhang, J. Wang, and R. G. Hilton (2016),  
980 Connectivity of earthquake-triggered landslides with the fluvial network: Implications for landslide  
981 sediment transport after the 2008 Wenchuan earthquake, *Journal of Geophysical Research: Earth  
982 Surface*, 121(4), 703-724, doi: 10.1002/2015jf003718.

983 Liu, F, B.H. Fu, S.H. Yang (2013) Quantitative estimation of the evacuation time of landslide mass and  
984 sediment induced by the 2008 Wenchuan great earthquake along the Minjiang River, Longmen Shan  
985 in east Tibet, *Chinese Journal of Geophysics*, 56(5), 1517–1525. (in Chinese with English abstract)

986 Liu-Zeng, J., L. Wen, M. Oskin, and L. S. Zeng (2011), Focused modern denudation of the Longmen  
987 Shan margin, eastern Tibetan Plateau, *Geochemistry Geophysics Geosystems*, 12, Q1107, doi:  
988 10.1029/2011gc003652.

989 Malamud, B. D., D. L. Turcotte, F. Guzzetti, and P. Reichenbach (2004), Landslides, earthquakes, and  
990 erosion, *Earth and Planetary Science Letters*, 229(1–2), 45-59, doi: 10.1016/j.epsl.2004.10.018.

991 Marc, O., N. Hovius, and P. Meunier (2016a), The mass balance of earthquakes and earthquake  
992 sequences, *Geophysical Research Letters*, 43(8), 3708-3716, doi: 10.1002/2016gl068333.

993 Marc, O., N. Hovius, P. Meunier, T. Gorum, and T. Uchida (2016b), A seismologically consistent  
 994 expression for the total area and volume of earthquake-triggered landsliding, *Journal of Geophysical*  
 995 *Research: Earth Surface*, 121(4), 2015JF003732, doi: 10.1002/2015jf003732.  
 996 Meunier, P., N. Hovius, and A. J. Haines (2007), Regional patterns of earthquake-triggered landslides  
 997 and their relation to ground motion, *Geophysical Research Letters*, 34(20), L20408, doi  
 998 10.1029/2007gl031337.  
 999 Molnar, P., and P. England (1990), Late Cenozoic uplift of mountain ranges and global climate change:  
 1000 chicken or egg?, *Nature*, 346(6279), 29-34, doi: 10.1038/346029a0.  
 1001 Molnar, P., W. R. Boos, and D. S. Battisti (2010), Orographic Controls on Climate and Paleoclimate of  
 1002 Asia: Thermal and Mechanical Roles for the Tibetan Plateau, *Annual Review of Earth and Planetary*  
 1003 *Sciences*, 38(1), 77-102, doi: 10.1146/annurev-earth-040809-152456.  
 1004 Montgomery, D. R., and M. T. Brandon (2002), Topographic controls on erosion rates in tectonically  
 1005 active mountain ranges, *Earth and Planetary Science Letters*, 201(3-4), 481-489, doi:  
 1006 10.1016/S0012-821X(02)00725-2.  
 1007 Ouimet, W. B. (2010), Landslides associated with the May 12, 2008 Wenchuan earthquake:  
 1008 Implications for the erosion and tectonic evolution of the Longmen Shan, *Tectonophysics*, 491(1-4),  
 1009 244-252, doi: 10.1016/j.tecto.2009.09.012.  
 1010 Ouimet, W. B., K. X. Whipple, and D. E. Granger (2009), Beyond threshold hillslopes: Channel  
 1011 adjustment to base-level fall in tectonically active mountain ranges, *Geology*, 37(7), 579-582, doi:  
 1012 10.1130/G30013a.1.  
 1013 Parker, R. N., A. L. Densmore, N. J. Rosser, M. de Michele, Y. Li, R. Q. Huang, S. Whadcoat, and D. N.  
 1014 Petley (2011), Mass wasting triggered by the 2008 Wenchuan earthquake is greater than orogenic  
 1015 growth, *Nature Geoscience*, 4(7), 449-452, doi: 10.1038/Ngeo1154.  
 1016 Raymo, M. E., W. F. Ruddiman, and P. N. Froelich (1988), Influence of late Cenozoic mountain  
 1017 building on ocean geochemical cycles, *Geology*, 16(7), 649-653, doi:  
 1018 10.1130/0091-7613(1988)016<0649:iolcmb>2.3.co;2.  
 1019 Reiners, P. W., and M. T. Brandon (2006), Using thermochronology to understand orogenic erosion,  
 1020 *Annual Reviews of Earth and Planetary Sciences*, 34, 419-466, doi:  
 1021 10.1146/annurev.earth.34.031405.125202.  
 1022 Richardson, N. J., A. L. Densmore, D. Seward, A. Fowler, M. Wipf, M. A. Ellis, L. Yong, and Y. Zhang  
 1023 (2008), Extraordinary denudation in the Sichuan Basin: Insights from low-temperature  
 1024 thermochronology adjacent to the eastern margin of the Tibetan Plateau, *Journal of Geophysical*  
 1025 *Research: Solid Earth*, 113(B4), doi: 10.1029/2006jb004739.  
 1026 Roback, K., M. Clark, A. J. West, D. Zekkos, G. Li, S. F. Gallen, D. Champlain, J. Godt (2017), The  
 1027 size, distribution, and mobility of landslides caused by the 2015  $M_w$ 7.8 Gorkha earthquake, Nepal,  
 1028 accepted, *Geomorphology*  
 1029 Shen, Z. K., J. B. Sun, P. Z. Zhang, Y. G. Wan, M. Wang, R. Burgmann, Y. H. Zeng, W. J. Gan, H. Liao,  
 1030 and Q. L. Wang (2009), Slip maxima at fault junctions and rupturing of barriers during the 2008  
 1031 Wenchuan earthquake, *Nature Geoscience*, 2(10), 718-724, doi: 10.1038/ngeo636.  
 1032 Steer, P., M. Simoes, R. Cattin, and J. B. H. Shyu (2014), Erosion influences the seismicity of active  
 1033 thrust faults, *Nature Communications*, 5, doi: 10.1038/ncomms6564.  
 1034 Thompson, T. B., A. Plesch, J. H. Shaw, and B. J. Meade (2015), Rapid slip-deficit rates at the eastern  
 1035 margin of the Tibetan Plateau prior to the 2008  $M_w$  7.9 Wenchuan earthquake, *Geophysical*  
 1036 *Research Letters*, 42(6), 1677-1684, doi: 10.1002/2014gl062833.

1037 Tian, Y., B. P. Kohn, A. J. W. Gleadow, and S. Hu (2013), Constructing the Longmen Shan eastern  
1038 Tibetan Plateau margin: Insights from low-temperature thermochronology, *Tectonics*, 32(3), 576-592,  
1039 doi: 10.1002/tect.20043.

1040 Utsu, T. (1999), Representation and Analysis of the Earthquake Size Distribution: A Historical Review  
1041 and Some New Approaches, *pure and applied geophysics*, 155(2), 509-535, doi:  
1042 10.1007/s000240050276.

1043 Vanmaercke, M., F. Ardizzone, M. Rossi, and F. Guzzetti (2017), Exploring the effects of seismicity on  
1044 landslides and catchment sediment yield: An Italian case study, *Geomorphology*, 278, 171-183, doi:  
1045 10.1016/j.geomorph.2016.11.010.

1046 Wang, E., E. Kirby, K. P. Furlong, M. van Soest, G. Xu, X. Shi, P. J. J. Kamp, and K. V. Hodges (2012),  
1047 Two-phase growth of high topography in eastern Tibet during the Cenozoic, *Nature Geoscience*, 5(9),  
1048 640-645, doi: 10.1038/ngeo1538.

1049 Wang, J., Z. Jin, R. G. Hilton, F. Zhang, A. L. Densmore, G. Li, and A. J. West (2015a), Controls on  
1050 fluvial evacuation of sediment from earthquake-triggered landslides, *Geology*, 43(2), 115-118, doi:  
1051 10.1130/g36157.1.

1052 Wang, J., Z. Jin, R. G. Hilton, F. Zhang, G. Li, A. L. Densmore, D. R. Gröcke, X. Xu, and A. J. West  
1053 (2016), Earthquake-triggered increase in biospheric carbon export from a mountain belt, *Geology*,  
1054 44(9), 44(9), doi: 10.1130/g37533.1.

1055 Wang, M., D. Jia, J. H. Shaw, J. Hubbard, A. Plesch, Y. Li, and B. Liu (2014), The 2013 Lushan  
1056 earthquake: Implications for seismic hazards posed by the Range Front blind thrust in the Sichuan  
1057 Basin, China, *Geology*, 42(10), 915-918, doi: 10.1130/g35809.1.

1058 Wang, Y., K. Zhang, Q. Gan, W. Zhou, L. Xiong, S. Zhang, and C. Liu (2015b), Bayesian probabilities  
1059 of earthquake occurrences in Longmenshan fault system (China), *Journal of Seismology*, 19(1),  
1060 69-82, doi: 10.1007/s10950-014-9451-2.

1061 West, A. J., R. Hetzel, G. Li, Z. Jin, F. Zhang, R. G. Hilton, and A. L. Densmore (2014), Dilution of  
1062 <sup>10</sup>Be in detrital quartz by earthquake-induced landslides: Implications for determining denudation  
1063 rates and potential to provide insights into landslide sediment dynamics, *Earth and Planetary Science  
1064 Letters*, 396(0), 143-153, doi: 10.1016/j.epsl.2014.03.058.

1065 Xu, C., X. Xu, X. Yao, and F. Dai (2014), Three (nearly) complete inventories of landslides triggered  
1066 by the May 12, 2008 Wenchuan Mw 7.9 earthquake of China and their spatial distribution statistical  
1067 analysis, *Landslides*, 11(3), 441-461, doi: 10.1007/s10346-013-0404-6.

1068 Xu, C., X. Xu, and J. B. H. Shyu (2015), Database and spatial distribution of landslides triggered by the  
1069 Lushan, China Mw 6.6 earthquake of 20 April 2013, *Geomorphology*, 248, 77-92, doi:  
1070 10.1016/j.geomorph.2015.07.002.

1071 Yang, S. L., K. H. Xu, J. D. Milliman, H. F. Yang, and C. S. Wu (2015), Decline of Yangtze River water  
1072 and sediment discharge: Impact from natural and anthropogenic changes, *Scientific reports*, 5, 12581,  
1073 doi: 10.1038/srep12581.

1074